Fission barriers in actinides in covariant density functional theory: The role of triaxiality

H. Abusara,[1] A. V. Afanasjev,[1] and P. Ring[2]

[1]*Department of Physics and Astronomy, Mississippi State University, Mississippi 39762, USA*
[2]*Fakultät für Physik, Technische Universität München, D-85748 Garching, Germany*
(Received 31 May 2010; published 6 October 2010)

Relativistic mean-field theory allowing for triaxial deformations is applied for a systematic study of fission barriers in the actinide region. Different pairing schemes are studied in detail and it is shown that covariant density functional theory is able to describe fission barriers on a level of accuracy comparable with nonrelativistic calculations, even with the best phenomenological macroscopic + microscopic approaches. Triaxiality in the region of the first saddle plays a crucial role in achieving that.

PACS number(s): 21.60.Jz, 24.75.+i, 27.90.+b

I. INTRODUCTION

A study of the (static) inner fission barrier heights B_f^{st} of even-even nuclei is motivated by the importance of this quantity for several physical phenomena. Many heavy nuclei decay by spontaneous fission, and the size of the fission barrier is a measure for the stability of a nucleus reflected in the spontaneous fission lifetimes of these nuclei [1]. The probability for the formation of a superheavy nucleus in a heavy-ion-fusion reaction is also directly connected to the height of its fission barrier [2]. The height B_f^{st} is a decisive quantity in the competition between neutron evaporation and fission of a compound nucleus in the process of its cooling. The large sensitivity of the cross section σ for the synthesis of the fissioning nuclei on the barrier height B_f^{st} stresses a need for accurate calculations of this value. For example, a change of B_f^{st} by 1 MeV changes the calculated survival probability of a synthesized nucleus by about one order of magnitude or even more [2]. The population and survival of hyperdeformed states at high spin also depends on the fission barriers [3,4]. In addition, the r process of stellar nucleosynthesis depends (among other quantities such as masses and β-decay rates) on the fission barriers of very neutron-rich nuclei [5,6].

During the last decade the role of triaxiality in the region of the saddle point of fission barriers was recognized and tested in many theoretical frameworks. It was found that the height of the barrier is reduced when triaxial shapes are allowed [7,8]. However, this lowering strongly depends on the proton and neutron numbers and on the model employed. The investigations of inner fission barriers with triaxiality included are available within the frameworks of the microscopic + macroscopic method [9–13], the extended Thomas-Fermi plus Strutinsky integral [14], and nonrelativistic energy density functionals based on Skyrme [7,15–17] and Gogny [8,18,19] forces.

Covariant density functional theory (CDFT) [20] is an approach alternative to the previously mentioned nonrelativistic methods. Built on Lorentz covariance and the Dirac equation, it provides a natural incorporation of spin degrees of freedom [21,22] and an accurate description of spin-orbit splittings [22] (see also Fig. 2 in Ref. [23]), which has an essential influence on the underlying shell structure. Lorentz covariance of the CDFT equations leads to the fact that time-odd mean fields of this theory are determined as spatial components of Lorentz

vectors and therefore coupled with the same constants as the timelike components [24] which are fitted to ground-state properties of finite nuclei. In addition, pseudospin symmetry finds a natural explanation in the relativistic framework [25]. Over the years a large variety of nuclear phenomena have been successfully described within the CDFT (see Ref. [20] and references therein).

However, the progress in the study of the fission barriers within CDFT was slower than in its nonrelativistic counterparts. Inner fission barriers in several nuclei have been calculated in the axially symmetric relativistic mean field (RMF) + BCS approach in Refs. [26–30]. However, these investigations employ the constant gap approximation in the BCS part. Our recent study of pairing schemes used for the calculations of fission barriers clearly shows that this approximation leads to unphysical results for the fission barriers [31]. Thus, the results of these works have to be treated with caution. Fission barriers have also been studied in axially symmetric RMF calculations within the BCS approximation using an effective density-dependent zero-range force in the pairing channel; this force represents a much more realistic approximation for pairing [31]. Recently, relativistic Hartree-Bogoliubov (RHB) calculations with the Gogny force D1S and with δ forces in the pairing channel also have been carried out [31] for a study of fission barriers with axial symmetry.

Unfortunately, axially symmetric calculations cannot be directly compared with experimental data because, as was shown in nonrelativistic calculations [7,8], the lowering of fission barriers due to triaxiality is significant and can reach 3–4 MeV in some nuclei. At present, no systematic studies of the effects of triaxial degrees of freedom on the height of inner fission barriers are available in the covariant density functional theory; this degree of freedom was only studied in specific nuclei such as ^{264}Hs [15] and ^{240}Pu [32] within the RMF + BCS approach as well as ^{240}Pu [33] within the RHB approach. Thus, the main goal of the current manuscript is to perform a systematic investigation of the inner fission barriers within the triaxial RMF + BCS approach, and for the first time to confront these important experimental quantities with CDFT in a systematic way.

The manuscript is organized as follows. The triaxial RMF + BCS theory and its details related to the calculations of fission barriers are discussed in Sec. II. Section III is devoted

to the analysis of the effects of the truncation of the basis in the particle-hole channel of the model. Truncation effects in the pairing channel are considered in Sec. IV. The results of the calculation of the fission barriers, the role of triaxiality, and the comparison with experiment are discussed in Sec. V. Finally, in Sec. VI, we report on calculations with other relativistic parameter sets based on density-dependent coupling constants and in Sec. VII summarize the results of our work.

II. THEORETICAL FRAMEWORK AND THE DETAILS OF NUMERICAL CALCULATIONS

The starting point of covariant density functional theory is a standard Lagrangian density [34],

$$
\begin{aligned}
\mathcal{L} = {} & \bar{\psi}[\gamma(i\partial - g_\omega\omega - g_\rho\vec{\rho}\vec{\tau} - eA) - m - g_\sigma\sigma]\psi \\
& + \tfrac{1}{2}(\partial\sigma)^2 - \tfrac{1}{2}m_\sigma^2\sigma^2 - \tfrac{1}{4}\Omega_{\mu\nu}\Omega^{\mu\nu} + \tfrac{1}{2}m_\omega^2\omega^2 \\
& - \tfrac{1}{4}\vec{R}_{\mu\nu}\vec{R}^{\mu\nu} + \tfrac{1}{2}m_\rho^2\vec{\rho}^{\,2} - \tfrac{1}{4}F_{\mu\nu}F^{\mu\nu},
\end{aligned}
\tag{1}
$$

which contains nucleons described by the Dirac spinors ψ with the mass m and several effective mesons characterized by the quantum numbers of spin, parity, and isospin. They create effective fields in a Dirac equation, which corresponds to the Kohn-Sham equation [35] in the nonrelativistic case.

The Lagrangian (1) contains as parameters the meson masses m_σ, m_ω, and m_ρ and the coupling constants g_σ, g_ω, and g_ρ. e is the charge of the protons and it vanishes for neutrons. This model was first introduced by Walecka [36,37]. It turned out that surface properties of finite nuclei cannot be described properly by this model. Therefore, Boguta and Bodmer [38] introduced a density dependence via a nonlinear meson coupling replacing the term $\frac{1}{2}m_\sigma^2\sigma^2$ in Eq. (1) by

$$
U(\sigma) = \tfrac{1}{2}m_\sigma^2\sigma^2 + \tfrac{1}{3}g_2\sigma^3 + \tfrac{1}{4}g_3\sigma^4.
\tag{2}
$$

If not specified otherwise, the calculations are performed with the NL3* parametrization of the RMF Lagrangian [39] shown in Table I. Apart from the fixed values for the masses $m = 939$ MeV, $m_\omega = 782.6$ MeV, and $m_\rho = 763$ MeV it contains six phenomenological parameters m_σ, g_σ, g_ω, g_ρ, g_2, and g_3, which were recently adjusted to the experimental data in finite nuclei [39] eliminating a few deficiencies of the well-known older parameter set NL3 [40].

In the current investigation, the triaxial RMF + BCS model is used [41]. The RMF equations are solved and at each step of the iteration the BCS occupation probabilities v_k^2 are determined. These quantities are used in the calculation of densities, energies, and new fields for the next step of the iteration. We

use monopole pairing force with the strength parameters G_τ for neutrons ($\tau = n$) and protons ($\tau = p$); this method is based on the residual interaction of the seniority model [42].

We start with a pairing strength parameter G and solve in each step of the iteration the gap equation [42],

$$
\frac{1}{G} = \sum_{k>0}\frac{1}{2E_k},
\tag{3}
$$

with $E_k = \sqrt{(\varepsilon_k - \lambda)^2 + \Delta^2}$, where ε_k are the eigenvalues of the Dirac equation and the chemical potential λ is determined by the average particle number. Then the occupation probabilities,

$$
v_k^2 = \frac{1}{2}\left(1 - \frac{\varepsilon_k - \lambda}{E_k}\right),
\tag{4}
$$

and the gap parameters,

$$
\Delta = G\sum_{k>0}u_k v_k,
\tag{5}
$$

are determined in a self-consistent way. The pairing energy is defined as

$$
E_{\text{pair}} = -\Delta\sum_{k>0}u_k v_k.
\tag{6}
$$

The sum over k in Eqs. (3), (5) and (6) run over all states in the pairing window $E_k < E_{\text{cutoff}}$.

In Ref. [43] empirical pairing gap parameters,

$$
\Delta_n^{\text{emp}} = \frac{4.8}{N^{1/3}}\,\text{MeV}, \qquad \Delta_p^{\text{emp}} = \frac{4.8}{Z^{1/3}}\,\text{MeV},
\tag{7}
$$

have been determined by the systematic fit to experimental data on neutron and proton gaps in the normal deformed minimum.

These empirical gap parameters form the basis for the definition of the strength parameters G_τ in the current manuscript. Two procedures have been used: (a) In the analysis of different truncation (Sec. III) and pairing schemes (Sec. IV), the values $G_n(Z,N)$ and $G_p(Z,N)$ are defined for each nucleus with neutron and proton number N and Z under study from the requirement that, in the normal deformed minimum, the calculated pairing gaps coincide with the empirical values. (b) In the systematic calculations of potential energy surfaces and fission barriers in actinides the same procedure is used first for all even-even nuclei in the $Z = 90$–100 and $N - Z = 42$–66 ranges resulting in a set of the strengths $G_n(Z,N)$ and $G_p(Z,N)$. Then, the following expressions [44]:

$$
A \cdot G_n = G_1^n - G_2^n\frac{N-Z}{A}\,\text{MeV},
\tag{8}
$$

$$
A \cdot G_p = G_1^p + G_2^p\frac{N-Z}{A}\,\text{MeV},
\tag{9}
$$

are used in the calculations. The parameters G_1^n, G_2^n, G_1^p, and G_2^p are defined by the least-square fit to the set of the $G_n(Z,N)$ and $G_p(Z,N)$. Their values depend on the parameter set of the Lagrangian and they are given in Table II. In this way we have strength parameters for the effective pairing interaction depending in a smooth way on the neutron and proton numbers and, because of the changing level density, the gap parameters derived from those values show fluctuations as a function of the particle numbers.

TABLE I. Parameters of the effective interaction NL3* in the RMF Lagrangian.

Parameters of NL3*	
$m = 939$ (MeV)	
$m_\sigma = 502.5742$ (MeV)	$g_\sigma = 10.0944$
$m_\omega = 782.600$ (MeV)	$g_\omega = 12.8065$
$m_\rho = 763.000$ (MeV)	$g_\rho = 4.5748$
$g_2 = -10.8093$ (fm^{-1})	
$g_3 = -30.1486$	

TABLE II. The G_1^n, G_2^n, G_1^p, and G_2^p parameters (in MeV) for different parametrizations of the RMF Lagrangian and cutoff energy $E_{cutoff} = 120$ MeV.

Force	G_1^n	G_2^n	G_1^p	G_2^p
NL3*	9.1	6.4	8.1	10.0
DD-PC1	9.2	5.4	8.0	11.4
DD-ME2	9.2	5.8	8.1	11.2

The calculations are performed imposing constraints on the axial and triaxial mass quadrupole moments. The method of quadratic constraints uses a variation of the function,

$$\langle H \rangle + \sum_{\mu=0,2} C_{2\mu}(\langle \hat{Q}_{2\mu} \rangle - q_{2\mu})^2, \tag{10}$$

where $\langle H \rangle$ is the total energy, and $\langle \hat{Q}_{2\mu} \rangle$ denotes the expectation values of the mass quadrupole operators,

$$\hat{Q}_{20} = 2z^2 - x^2 - y^2, \tag{11}$$
$$\hat{Q}_{22} = x^2 - y^2. \tag{12}$$

In these equations, $q_{2\mu}$ is the constrained value of the multipole moment, and $C_{2\mu}$ the corresponding stiffness constants [42].

Correlations beyond mean field can influence the calculated values of fission barrier height and the excitation energies of the superdeformed minima associated with the fission isomer [45]. The inclusion of rotational correlations can be performed by a symmetry restoration (angular momentum projection) and that of vibrations by a mixing of mean-field states corresponding to different shapes by the method of generator coordinates (GCM). So far such an investigation was performed only for ^{240}Pu within the generator coordinate method based on Skyrme DFT under the restriction to axially symmetric shapes [45]. It was found that compared to the ground state, angular momentum projection lowers the (axial) inner barrier by about 0.6 MeV and the fission isomer by about 1 MeV. In addition, it was found in Ref. [45] that the schematic rotational correction based on the Belyaev moment of inertia [46] frequently used in the literature gives a reduction of the fission barrier height which is appreciably larger than the one from angular momentum projection. Based on these results, no rotational corrections are taken into account in our calculations. A similar approach was used in the very successful calculations of Ref. [12].

In the current investigation we do not consider the outer fission barriers. However, this restriction has its own merits. The inner barriers are generally better measured than the outer ones, and they are certainly more important for the r process because they determine thresholds. Furthermore, spontaneous fission lifetimes tend to be dominated by the inner barrier, even if occasionally an outer barrier can have a crucial effect if it is wide enough. The consideration of only inner fission barriers allows us to restrict our calculations to reflection symmetric shapes, because the odd-multipole deformations (octupole, etc.) do not play a role in the inner fission barrier of the actinides and superheavy nuclei [10,17,27,47,48]. However, the analysis of the symmetric fission pathway, which is the lowest in energy in heavy actinide nuclei such as some Fm isotopes (see Refs. [7,15]), is also possible in the current framework.

III. TRUNCATION EFFECTS IN THE PARTICLE-HOLE CHANNEL

The RMF + BCS equations are solved in the basis of an anisotropic three-dimensional harmonic oscillator in Cartesian coordinates characterized by the deformation parameters β_0 and γ_0 and the oscillator frequency $\hbar\omega_0 = 41A^{-1/3}$ MeV (see Refs. [41,49] for details). The deformation parameters of the oscillator basis β_0 and γ_0 are selected to be close to expected values β_2 and γ of constrained solution; this improves the convergence and minimizes the computational time. The truncation of the basis is performed in such a way that all states belonging to the shells up to N_F fermionic shells and N_B bosonic shells are taken into account. The computational time increases considerably with the increase of N_F, but it is much less dependent on N_B. Thus, special attention was paid to the selection of N_F of the basis to be chosen for a systematic study of fission barriers for the nuclei of interest, which provides at the same time a reasonable numerical accuracy in the predictions of the physical observables.

The selection of the truncation scheme was guided by the detailed analysis of the convergence performed in axially symmetric RMF + BCS and RHB calculations of Ref. [31]. In this reference, extensive tests of numerical convergence have been performed in the spherical, normal deformed, and superdeformed ($\beta_2 \sim 0.7-1.0$) minima in the RMF calculations without pairing on the example of the nuclei ^{238}U and ^{304}120 with $Z = 120$ and $N = 184$. Contrary to the previous studies of the convergence in the RMF framework which were based on the comparison of the N_F and $N_F + 2$ results, the "exact" solution (extending the calculations up to $N_F = 36$, $N_B = 36$) was defined. Then it was shown that the binding energies and inner fission barriers for $N_F = 20$ and $N_B = 20$ were described with an accuracy of approximately 200 and 100 keV, respectively, as compared with the exact solution. Therefore, the systematic calculations in the present manuscript have been carried out with $N_F = 20$ and $N_B = 20$. This selection of the basis is in line with our previous convergence tests in different mass regions (see, e.g., Ref. [4]) which clearly show that at large deformations full convergence of the binding energies is reached at larger values of N_F than at lower deformations. In addition, they show that larger sizes of the basis (larger N_F and N_B values) are needed for the nuclei with larger proton Z and neutron N numbers (see Refs. [24,49,50]).

Of course, as long as the same number of fermionic shells N_F and the same deformation of the basis β_0 is used, calculations with the axial code should give identical results to those obtained with the triaxial code at $\gamma = 0°$. In fact, for nuclei under study we find agreement with an accuracy of approximately 50 keV throughout the deformation range of interest, which is caused by small differences in the mesh points of the Gaussian integrations for the matrix elements. As a result, for axially symmetric shapes, the fission barrier heights which depend on the relative energies of the saddle point and normal deformed minimum differ by less than 50 keV in these two calculations.

Extensive convergence tests in axially symmetric Skyrme-Hartree-Fock calculations also show that a similar size of the basis is needed (see Sec. II B in Ref. [48] for more details).

The comparison of these convergence tests suggests that there is no big difference in the convergence of total energies as a function of the size of basis in the relativistic and nonrelativistic approaches.

Because the fermionic basis contains large and small components of the Dirac spinor, the diagonalization of the Dirac equation is by a factor of approximately 8 more time-consuming than the corresponding Schrödinger equation in the nonrelativistic case. As a consequence, triaxial RMF + BCS calculations are more computationally demanding than the ones performed in the triaxial Skyrme EDF with BCS approximation of Ref. [7]. This is also a reason why we treat the pairing channel in the present triaxial RMF calculations in the BCS approximation despite the fact that the triaxial cranked relativistic Hartree + Bogoliubov approach was developed in the end of the nineties [51–53] and successfully applied to the description of rotational structures in the pairing regime in different mass regions [51–55]. The RMF + BCS calculations are less time-consuming than the RHB calculations. In addition, as follows from our experience of the calculations in axially deformed RMF + BCS and RHB codes [31], the RMF + BCS calculations are more stable (especially, in the saddle point region) than the RHB calculations.

IV. TRUNCATION EFFECTS IN THE PAIRING CHANNEL

It is rather customary to analyze the dependence of total binding energies (or other physical observables) on the truncation of basis (see Sec. III). However, we were not able to find any detailed investigation where the impact of the size of the oscillator basis on the parameters of pairing in the BCS framework was discussed in detail. Thus, we studied the dependence of the strength of the pairing interaction on the number N_F of fermionic shells under the condition that the proton and neutron pairing gaps in the normal deformed minimum are fixed for all values of N_F and cutoff energies E_{cutoff}.

RMF + BCS calculations in the normal deformed minimum have been performed with several values of the cutoff energy E_{cutoff} in Eq. (5), namely $E_{cutoff} = 30$, 60, and 120 MeV. In addition, the prescription of Ref. [56] [indicated as "Eq. (13)" in the figures] was used. This prescription introduces smooth energy-dependent cutoff weights [57],

$$f_k = \frac{1}{1 + \exp[(\epsilon_k - \lambda_\tau - \Delta E_\tau)/\mu_\tau]}, \quad (13)$$

for the evaluation of the local pair density. In this equation, ϵ_k are the eigenvalues of the Dirac equation and the chemical potentials λ_τ of the proton ($\tau = p$) or neutron ($\tau = n$) subsystems are determined by the particle numbers N_τ. The cutoff parameters ΔE_τ and $\mu_\tau = \Delta E_\tau/10$ are chosen self-adjusting to the actual level density in the vicinity of the Fermi energy. ΔE_τ is fixed from the condition that the sum of the cutoff weights includes approximately one additional shell of single-particle states above the Fermi surface,

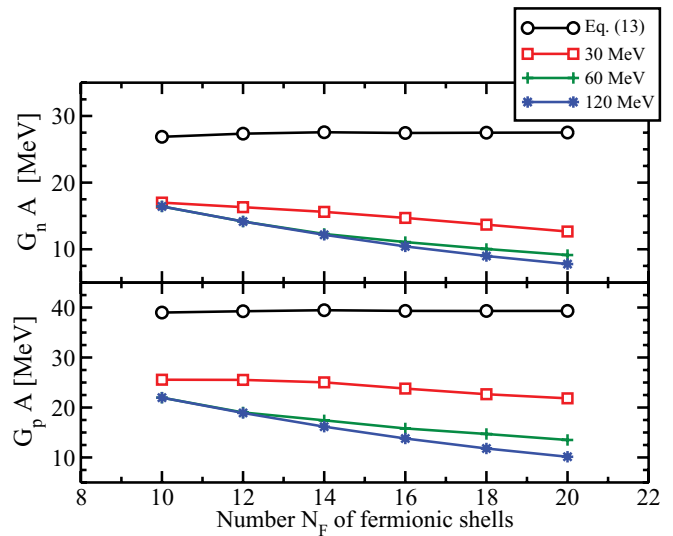$$\sum_{k \in \Omega_\tau} f_k = N_\tau + 1.65 \, N_\tau^{2/3}. \quad (14)$$

FIG. 1. (Color online) Neutron and proton pairing strengths as a function of number N_F of fermionic shells for different pairing schemes. Pairing schemes are indicated either by cutoff energy E_{cutoff} or by Eq. (13).

In Eq. (14), Ω_τ denotes the single-particle space used in the calculations.

Figures 1–3 summarize the results of this study for the normal deformed ground state in ^{236}Pu. One can see in Fig. 1 that the strengths of the pairing interaction depends not only on the cutoff energy E_{cutoff} but also on the number N_F of fermionic shells employed in the calculations. This dependence is very weak for the prescription of Ref. [56] because here the effective pairing window is quite small being around 7 MeV. On the other hand, the dependence of the pairing strength on N_F increases with the increase of E_{cutoff}. This can be understood in the following way: an increase of N_F brings more single-particle states into the pairing window,
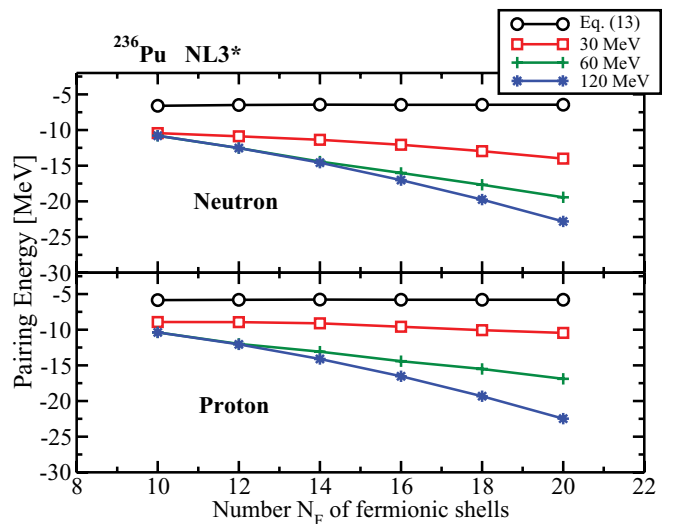

FIG. 2. (Color online) Neutron and proton pairing energies in the normal deformed minimum as a function of number N_F of fermionic shells for different pairing schemes.
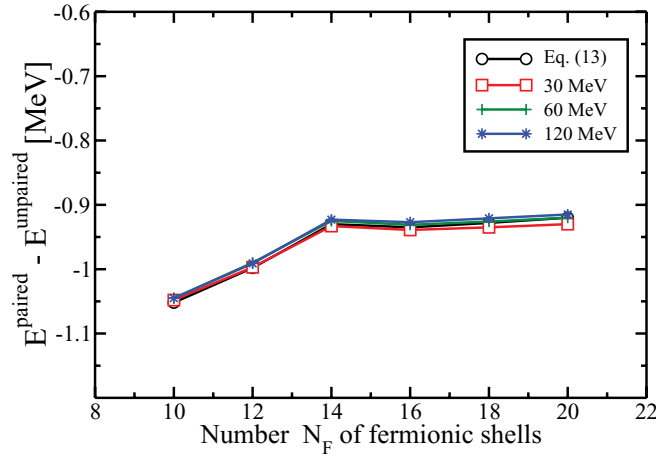
FIG. 3. (Color online) The dependence of additional binding due to pairing on the number N_F of major fermionic shells for different pairing schemes.

FIG. 5. (Color online) The same as in Fig. 4 but for ^{250}Cf.

thus, effectively requiring the decrease of pairing strength to keep the pairing gap fixed. This effect becomes more pronounced for larger pairing windows, which explains the steeper decrease of the pairing strength as a function of N_F with increasing E_{cutoff}.

The dependence of proton and neutron pairing energies E_{pair}^p and E_{pair}^n on the cutoff energy E_{cutoff} and on the number N_F of fermionic shells employed in the calculations is shown in Fig. 2. These energies depend only weakly on N_F in the case of the prescription of Ref. [56] because of the small effective pairing window. However, similar to the pairing strengths the dependence of pairing energies on N_F increases significantly with increasing E_{cutoff}. The origin of this feature is the same as in the case of the pairing strengths; it is discussed previously.

Note, however, that the dramatic changes in the pairing energy cannot be seen directly in the change of the energy, because they are compensated to some extent by the fact that the larger pairing seen in pairing energies causes a wider
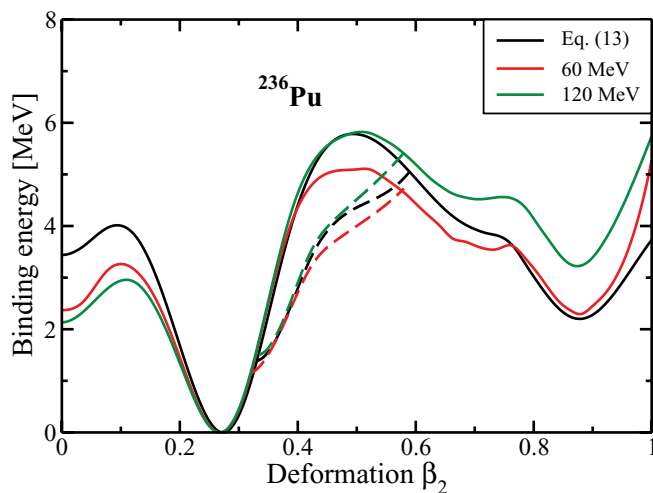
distribution of the occupation probabilities v_k^2 around the Fermi surface. Therefore, we study in Fig. 3 the energy difference between the binding energies $E^{\text{pair}} - E^{\text{unpair}}$ obtained in two self-consistent calculations with and without pairing. It turns out that for $N_F \geqslant 14$ this difference, whicht reflects the real physical impact of pairing, is smaller than 1 MeV and it neither depends on the cutoff energy E_{cutoff} nor on the value of N_F. Somewhat different values of $E^{\text{pair}} - E^{\text{unpair}}$ at lower N_F values are due to the fact that at these values of N_F the effects of the truncation of basis in the particle-hole channel have not been eliminated (see Sect. III for detail).

In Figs. 4 and 5 we compare the deformation energy curves for three different pairing schemes for the nuclei ^{236}Pu and

FIG. 4. (Color online) The dependence of fission barrier in ^{236}Pu on the pairing scheme. Solid and dashed lines are used for axially symmetric and triaxial solutions, respectively.
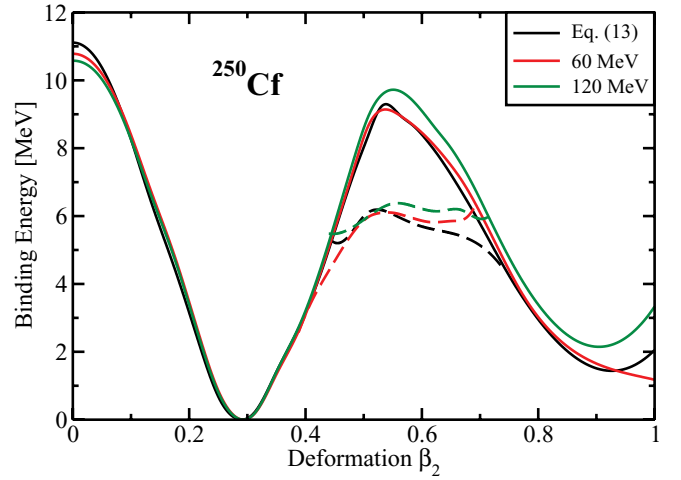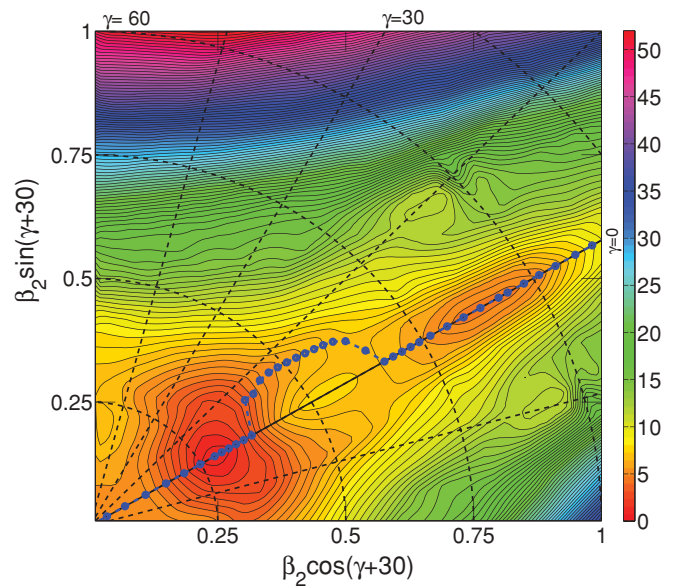

FIG. 6. (Color online) Potential energy surface in ^{240}Pu. The energy difference between two neighboring equipotential lines is equal to 0.5 MeV. The blue dashed line with solid circles shows the lowest in energy solution as a function of β_2. Further details are given in the text.
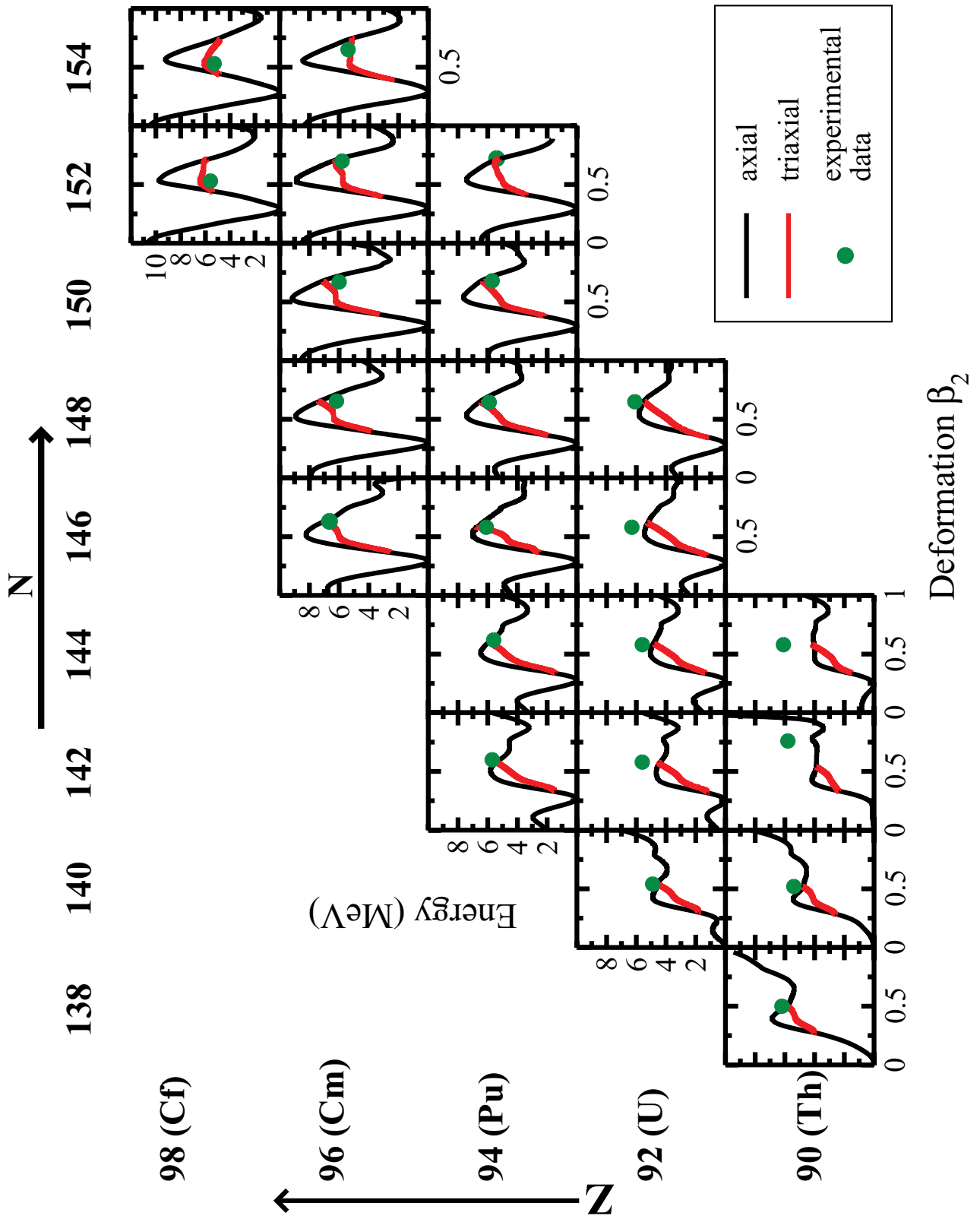
FIG. 7. (Color online) Deformation energy curves of even-even actinide nuclei obtained in the RMF + BCS calculations with the NL3*
parametrization. Black solid lines display the deformation energy curves for the axially symmetric solution, whereas red solid lines show the
deformation energy curves along the triaxial part of the fission path. Solid green circles show the experimental values of the height of inner
fission barrier. Experimental data are taken from Table IV in Ref. [48]. A typical uncertainty in the experimental values, as suggested by the
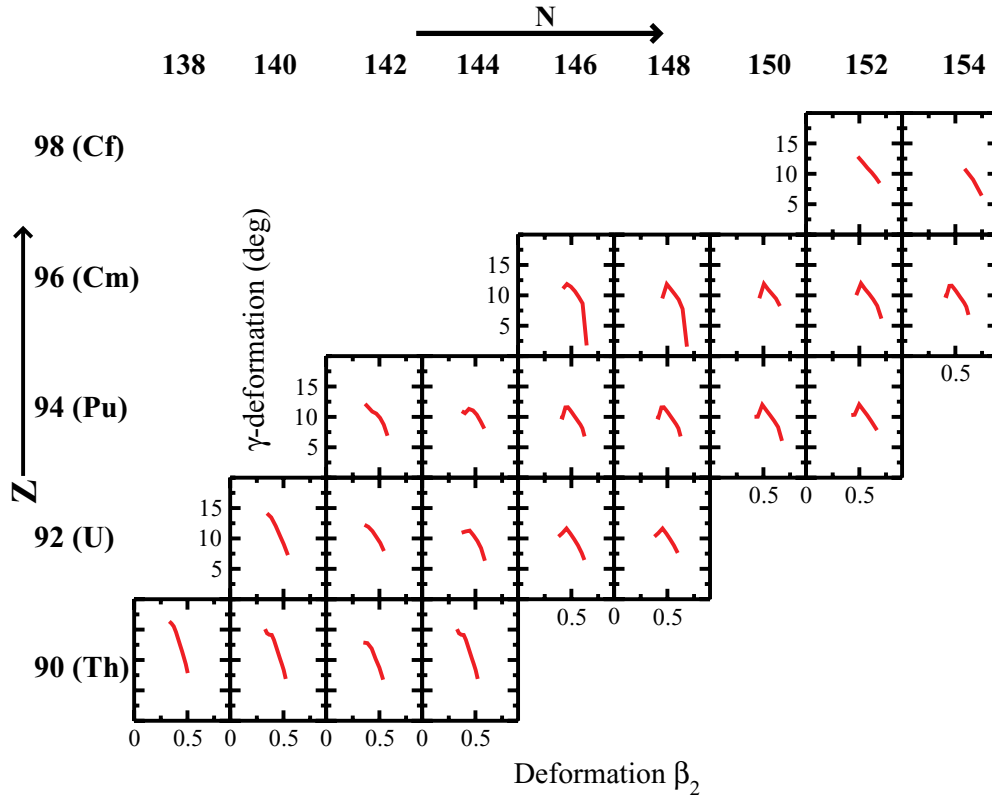differences among various compilations, is of the order of ± 0.5 MeV [48].

FIG. 8. (Color online) The γ deformations for the results of calculations shown by red lines in Fig. 7.
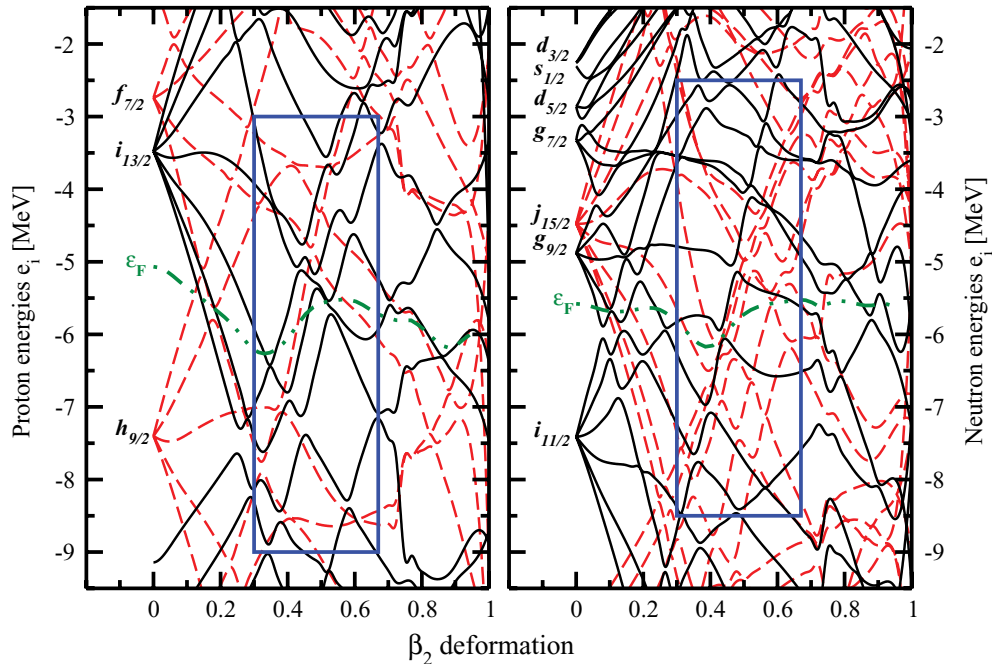

FIG. 9. (Color online) Proton and neutron single-particle energies in ^{242}Pu as a function of the quadrupole deformation β_2 for the axially symmetric solution. Solid (black) and dashed (red) lines are used for positive and negative parity states, respectively. Blue boxes show the regions that are displayed in more details in Fig. 10 below. Fermi energies ε_F are shown by dot-dot-dashed (green) lines.
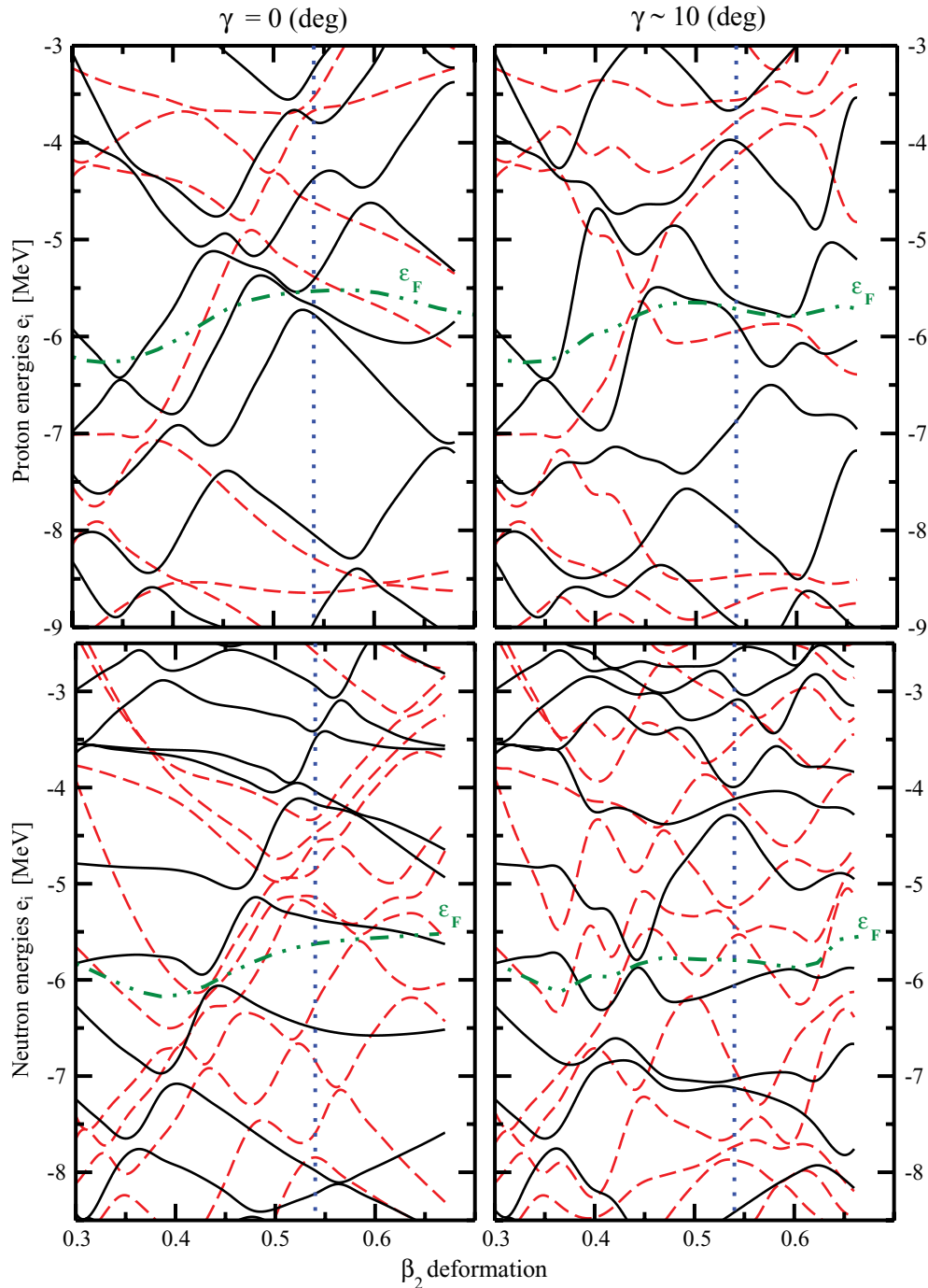
FIG. 10. (Color online) A comparison of proton and neutron single-particle energies at axially symmetric (left panels) and triaxial (right panels) solutions. The same notation for the lines as in Fig. 9 is used. Vertical blue dotted lines are used to show the deformation of the saddle point obtained in the axially symmetric solution.

^{250}Cf. The deformation energy curve for the axially symmetric solution is obtained as the $\gamma = 0°$ cross section of the potential energy surface. The deformation energy curve for the triaxial solution is obtained by the minimization of the potential energy surface along the β_2 direction. We show the deformation energy curve for the triaxial solution only in the range of β_2 values where it is lower in energy than the deformation energy curve of the axially symmetric solution. Note that

the potential energy surfaces are normalized to zero at the normal deformed minimum. As discussed in Ref. [31] we can see that these different schemes predict somewhat different fission barriers. In the systematic calculations presented in the following sections, we use the cutoff energy $E_{cutoff} = 120$ MeV. The selection of this value is based on the results of Ref. [31], where it was shown that the difference in the height of fission barriers obtained in the RHB calculations with finite

range D1S Gogny force and zero-range δ-force is minimal when the cutoff energy $E_{cutoff} = 120$ MeV is used (see Fig. 6 in Ref. [31]).

V. SYSTEMATIC ANALYSIS OF THE INNER FISSION BARRIERS

In this section we carry out a systematic investigation of fission barriers of even-even nuclei in the actinide region based on the parameter set NL3* and the pairing strength parameters given in Table II. In Fig. 6 we show as an example the potential energy surface of the nucleus ^{240}Pu in the β-γ plane. For axial symmetry we find the normal deformed minimum of the ground state at a deformation $\beta \sim 0.28$, a maximum at $\beta \sim 0.52$, and a superdeformed minimum at $\beta \sim 0.96$. We observe that the fission path (the part of the blue dashed line between normal and superdeformed minima) bypasses the axial barrier between the normal and superdeformed minima. The barrier height is determined by the maximum of the energy along this fission path.

The deformation energy curves for other even-even nuclei in this region obtained in these calculations are shown in Fig. 7. Full black lines show axially symmetric solutions, whereas we show the values of the deformation energy curves along the triaxial fission path by red full curves. One can see that by allowing for triaxial deformation the fission barrier heights are reduced by 1–4 MeV as compared with axially symmetric solutions. This lowering depends on the proton and neutron numbers. It also brings in average the results of the calculations in closer agreement with experimental data shown by green solid circles in Fig. 7. These circles display the height of the experimental fission barrier at the calculated β deformation of the saddle point. The calculated γ deformations of the triaxial parts of the fission path are shown in Fig. 8. On average they are close to 10°.

The microscopic origin of the lowering of the barrier due to triaxiality can be traced back to the changes of the level density in the vicinity of the Fermi level induced by triaxiality. Figure 9 shows the Nilsson diagrams for protons and neutrons for the axially symmetric solution in ^{242}Pu. The blue boxes in these diagrams define the deformation and energy ranges in which the axially symmetric and triaxial solutions are compared in Fig. 10. The lower (upper) deformation in these boxes corresponds to the deformation range over which the triaxial solution (red curve in Fig. 7) is lower in energy than the corresponding axially symmetric solution (black curve in Fig. 7). The lower and upper energy values in these boxes are defined approximately as $\varepsilon_F \pm 3$ MeV.

Proton and neutron single-particle energies within these deformation and energy ranges are shown for axially symmetric and triaxial solutions in Fig. 10. One can see that the single-particle level density at the Fermi level is lower for triaxial solutions than for axially symmetric solutions. This is especially clear at the deformation corresponding to the saddle point of the axially symmetric solution (indicated by vertical dotted blue lines in Fig. 10) that corresponds to a maximal level density and maximal pairing correlations. A lowering
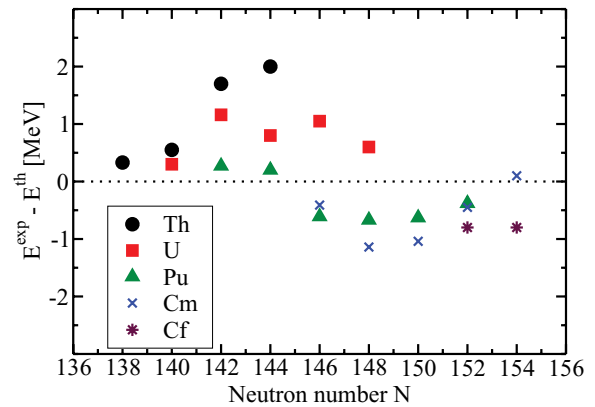

FIG. 11. (Color online) The difference between experimental and calculated heights of inner fission barriers as a function of neutron number N.

of the level density at the Fermi surface leads to a more negative shell correction energy (as compared with axially symmetric solution), and, as a consequence, to a lower fission barrier. This is in agreement with the analysis of Ref. [10] that also attributes the lowering of the inner fission barrier due to triaxiality to the microscopic (shell correction) part of the macroscopic + microscopic model. A similar mechanism is responsible for the lowering of the asymmetric saddle with respect to the symmetric saddle at the outer fission barrier (see Sect. VI in Ref. [12]).

Figures 11 and 12 show the differences between calculated and experimental heights of inner fission barriers. The average deviation between theory and experiment is 0.76 MeV. This is comparable with the results obtained in the macroscopic + microscopic method (see Sec. IV C and Fig. 11 in Ref. [11] and Sec. VII A in Ref. [12]) which describe experimental fission barriers with an average error of around 1 MeV.

It is necessary, however, to say that neither proton nor neutron particle number dependencies of fission barrier height are completely reproduced in these calculations. This is clearly seen in Figs. 11 and 12. However, the same problem also exists in macroscopic + microscopic calculations (see Fig. 11
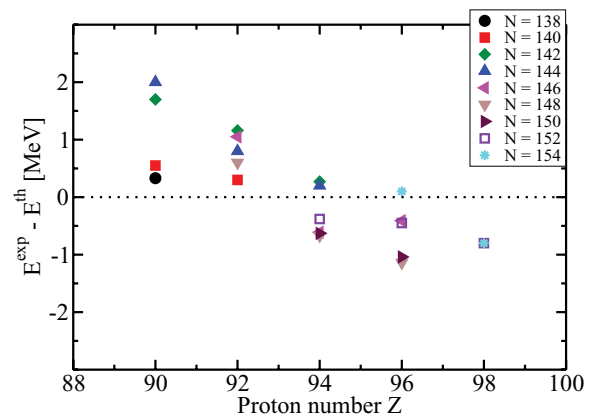

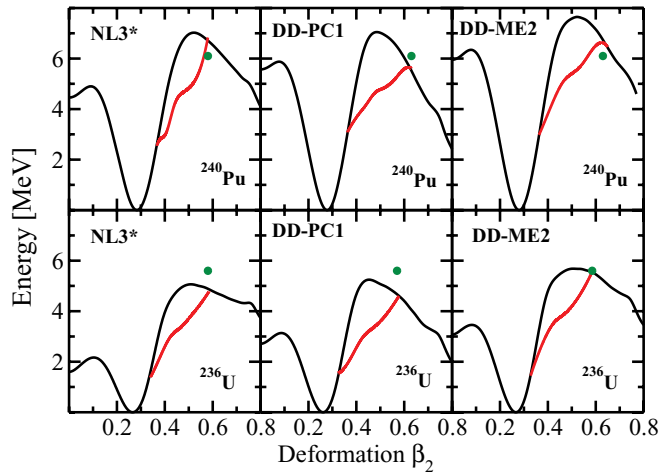FIG. 12. (Color online) The same as in Fig. 11 but as a function of proton number Z.

FIG. 13. (Color online) The same as in Fig. 7 but for fission barriers in ^{240}Pu and ^{236}U obtained in the calculations with the NL3*, DD-ME2, and DD-PC1 parametrizations of the RMF Lagrangian.

in Ref. [11] and Figs. 23–32 in Ref. [12]). There are very few energy density functional calculations of the fission barriers with triaxiality included, and neither of them confronts in a systematic way experimental data in actinides. However, limited results in the Skyrme EDF presented in Ref. [16] show similar unresolved particle number dependencies for the inner fission barrier heights.

VI. RESULTS FOR THE PARAMETER SETS DD-ME2 AND DD-PC1

To investigate to what extent our results depend on the density functional under investigation we performed also an analysis of the fission barriers of the two nuclei ^{240}Pu and ^{236}U using the parameter sets DD-ME2 [58] and DD-PC1 [59]. The first is representative of the class of the RMF models [58,60] where the nucleus is described as a system of Dirac nucleons interacting via the exchange of mesons with finite masses leading to interactions of finite range. An explicit density dependence for the meson-nucleon vertices is used. The DD-PC1 parametrization belongs to the class of the RMF models in which the finite-range meson exchange is replaced

by zero-range interactions with density-dependent coupling constants and derivative terms [59,61,62].

In Fig. 13 we compare the deformation energy curves of ^{240}Pu and ^{236}U obtained in the calculations with the three parameter sets NL3*, DD-PC1, and DD-ME2 of the RMF Lagrangian. Although there are some differences between the deformation energy curves obtained in the calculations with different parametrizations, in general, they show the same features. In addition, calculated fission barrier heights reasonably agree with experimental data. More systematic investigations of fission barriers with the DD-ME2 and DD-PC1 parametrizations of the RMF Lagrangian are in progress and their results will be presented in a forthcoming manuscript.

VII. CONCLUSIONS

We presented here the first systematic investigation of triaxial fission barriers in the actinide region within covariant density functional theory. The calculations have been carried out with the parameter set NL3* and they have been compared in specific cases also with the results of parameter sets DD-ME2 and DD-PC1. Pairing correlations are taken into account in the BCS approximation using seniority zero forces adjusted to empirical values of the gap parameters. It is found that with only one exception (^{234}Th) in all the nuclei under investigation the height of the inner fission barrier is reduced by allowing for triaxial deformations by $1-4$ MeV. The fission path avoids a maximum of the axially symmetric potential energy surface between the first and the second minimum by going through a valley in the (β, γ) plane with a triaxial deformation $\gamma \approx 10°$. A systematic comparison of our results with experimentally determined fission barriers in this region shows reasonable agreement with data comparable with the best macroscopic + microscopic calculations.

[1] A. Sobiczewski and K. Pomorski, Prog. Part. Nucl. Phys. **58**, 292 (2007).

[2] M. G. Itkis, Y. T. Oganessian, and V. I. Zagrebaev, Phys. Rev. C **65**, 044602 (2002).

[3] J. Dudek, K. Pomorski, N. Schunck, and N. Dubray, Eur. Phys. J. A **20**, 15 (2004).

[4] A. V. Afanasjev and H. Abusara, Phys. Rev. C **78**, 014315 (2008).

[5] M. Arnould and K. Takahashi, Rep. Prog. Phys. **62**, 395 (1999).

[6] A. Mamdouh, J. M. Pearson, M. Rayet, and F. Tondeur, Nucl. Phys. A **679**, 337 (2001).

[7] A. Staszczak, A. Baran, J. Dobaczewski, and W. Nazarewicz, Phys. Rev. C **80**, 014309 (2009).

[8] M. Warda, J. L. Egido, L. M. Robledo, and K. Pomorski, Phys. Rev. C **66**, 014310 (2002).

[9] P. Möller, A. J. Sierk, and A. Iwamoto, Phys. Rev. Lett. **92**, 072501 (2004).

[10] A. Sobiczewski and M. Kowal, Phys. Scr., T **125**, 68 (2006).

[11] A. Dobrowolski, K. Pomorski, and J. Bartel, Phys. Rev. C **75**, 024613 (2007).

[12] P. Möller, A. J. Sierk, T. Ichikawa, A. Iwamoto, R. Bengtsson, H. Uhrenholt, and S. Åberg, Phys. Rev. C **79**, 064304 (2009).

[13] A. Dobrowolski, B. Nerlo-Pomorska, K. Pomorski, and J. Bartel, Acta Phys. Pol. B **40**, 705 (2009).

[14] A. K. Dutta, J. M. Pearson, and F. Tondeur, Phys. Rev. C **61**, 054303 (2000).

[15] M. Bender, K. Rutz, P.-G. Reinhard, J. A. Maruhn, and W. Greiner, Phys. Rev. C **58**, 2126 (1998).

[16] L. Bonneau, P. Quentin, and D. Samsoen, Eur. Phys. J. A **21**, 391 (2004).

[17] A. Staszczak, J. Dobaczewski, and W. Nazarewicz, Acta Phys. Pol. B **38**, 1589 (2007).

[18] M. Warda, Eur. Phys. J. A **42**, 605 (2009).

[19] R. Rodríguez-Guzmán, P. Sarriguren, L. M. Robledo, and J. E. Garcia-Ramos, Phys. Rev. C **81**, 024310 (2010).

[20] D. Vretenar, A. V. Afanasjev, G. A. Lalazissis, and P. Ring, Phys. Rep. **409**, 101 (2005).

[21] P.-G. Reinhard, Rep. Prog. Phys. **52**, 439 (1989).

[22] P. Ring, Prog. Part. Nucl. Phys. **37**, 193 (1996).

[23] M. Bender, K. Rutz, P.-G. Reinhard, J. A. Maruhn, and W. Greiner, Phys. Rev. C **60**, 034304 (1999).

[24] A. V. Afanasjev and H. Abusara, Phys. Rev. C **81**, 014309 (2010).

[25] J. N. Ginocchio, Phys. Rev. Lett. **78**, 436 (1997).

[26] V. Blum, J. Maruhn, P.-G. Reinhard, and W. Greiner, Phys. Lett. B **323**, 262 (1994).

[27] K. Rutz, J. A. Maruhn, P.-G. Reinhard, and W. Greiner, Nucl. Phys. A **590**, 680 (1995).

[28] Z. Ren, F. Tai, and D.-H. Chen, Phys. Rev. C **66**, 064306 (2002).

[29] W. Zhang, S.-S. Zhang, S.-Q. Zhang, and J. Meng, Chin. Phys. Lett. **20**, 1694 (2003).

[30] W. H. Long, N. Van Giai, and J. Meng, Phys. Lett. B **640**, 150 (2006).

[31] S. Karatzikos, A. V. Afanasjev, G. A. Lalazissis, and P. Ring, Phys. Lett. B **689**, 72 (2010).

[32] M. Bender, P.-H. Heenen, and P.-G. Reinhard, Rev. Mod. Phys. **75**, 121 (2003).

[33] Z. P. Li, T. Nikšić, D. Vretenar, P. Ring, and J. Meng, Phys. Rev. C **81**, 064321 (2010).

[34] Y. K. Gambhir, P. Ring, and A. Thimet, Ann. Phys. (NY) **198**, 132 (1990).

[35] W. Kohn and L. J. Sham, Phys. Rev. **137**, A1697 (1965).

[36] J. D. Walecka, Ann. Phys. (NY) **83**, 491 (1974).

[37] B. D. Serot and J. D. Walecka, Adv. Nucl. Phys. **16**, 1 (1986).

[38] J. Boguta and A. R. Bodmer, Nucl. Phys. A **292**, 413 (1977).

[39] G. A. Lalazissis, S. Karatzikos, R. Fossion, D. Peña Arteaga, A. V. Afanasjev, and P. Ring, Phys. Lett. B **671**, 36 (2009).

[40] G. A. Lalazissis, J. König, and P. Ring, Phys. Rev. C **55**, 540 (1997).

[41] W. Koepf and P. Ring, Nucl. Phys. A **493**, 61 (1989).

[42] P. Ring and P. Schuck, *The Nuclear Many-Body Problem* (Springer-Verlag, Berlin, 1980).

[43] P. Möller and J. Nix, Nucl. Phys. A **536**, 20 (1992).

[44] J. Dudek, A. Majhofer, and J. Skalski, J. Phys. G **6**, 447 (1980).

[45] M. Bender, P.-H. Heenen, and P. Bonche, Phys. Rev. C **70**, 054304 (2004).

[46] S. T. Belyaev, Mat. Fys. Medd. Dan. Vid. Selsk. **31**, 11 (1959).

[47] S. Ćwiok, J. Dobaczewski, P.-H. Heenen, P. Magierski, and W. Nazarewicz, Nucl. Phys. A **611**, 211 (1996).

[48] M. Samyn, S. Goriely, and J. M. Pearson, Phys. Rev. C **72**, 044316 (2005).

[49] A. V. Afanasjev, J. König, and P. Ring, Nucl. Phys. A **608**, 107 (1996).

[50] A. V. Afanasjev, I. Ragnarsson, and P. Ring, Phys. Rev. C **59**, 3166 (1999).

[51] A. V. Afanasjev, J. König, and P. Ring, Phys. Rev. C **60**, 051303(R) (1999).

[52] A. V. Afanasjev, P. Ring, and J. König, Nucl. Phys. A **676**, 196 (2000).

[53] A. V. Afanasjev, J. König, P. Ring, L. M. Robledo, and J. L. Egido, Phys. Rev. C **62**, 054306 (2000).

[54] A. V. Afanasjev, T. L. Khoo, S. Frauendorf, G. A. Lalazissis, and I. Ahmad, Phys. Rev. C **67**, 024309 (2003).

[55] A. V. Afanasjev and S. Frauendorf, Phys. Rev. C **71**, 064318 (2005).

[56] M. Bender, K. Rutz, P.-G. Reinhard, and J. A. Maruhn, Eur. Phys. J. A **8**, 59 (2000).

[57] S. J. Krieger, P. Bonche, H. Flocard, P. Quentin, and M. S. Weiss, Nucl. Phys. A **517**, 275 (1990).

[58] G. A. Lalazissis, T. Nikšić, D. Vretenar, and P. Ring, Phys. Rev. C **71**, 024312 (2005).

[59] T. Nikšić, D. Vretenar, and P. Ring, Phys. Rev. C **78**, 034318 (2008).

[60] S. Typel and H. H. Wolter, Nucl. Phys. A **656**, 331 (1999).

[61] B. A. Nikolaus, T. Hoch, and D. G. Madland, Phys. Rev. C **46**, 1757 (1992).

[62] T. Bürvenich, D. G. Madland, J. A. Maruhn, and P.-G. Reinhard, Phys. Rev. C **65**, 044308 (2002).